PAPER

Check for updates

Ferroelectric modulation of CuCo$_2$O$_4$ nanorods for controllable alkaline water electrolysis†

Ruixue Zhang,[a] Jing Wang,[a,b] Qiyan Sun,[a] Fuyuan Cao,[a] Guang-Rui Xu, [ID] *[a,c]
Yu Miao,[a] Chuanfang Zhang,[c] Zexing Wu [ID] [a,b] and Lei Wang [ID] *[a,b]

As a technology for emerging environmental applications, water electrolysis is a significant approach for producing clean hydrogen energy. In this work, we used an efficacious piezoelectric method to significantly improve the catalytic water splitting activity without affecting the morphology as well as the components by altering the bulk charge separation state inside the material. The obtained CuCo$_2$O$_4$ nanorods were treated under a corona polarization apparatus, which significantly enhanced ferroelectricity relative to that before the polarization increasing the physical charge separation and piezoelectric potential energy, enhancing the green hydrogen production. The polarized CuCo$_2$O$_4$ nanorods exhibit excellent water electrolysis performance under alkaline conditions, with hydrogen evolution overpotential of 78.7 mV and oxygen evolution overpotential of 299 mV at 10 mA cm^{-2}, which is much better than that of unpolarized CuCo$_2$O$_4$ nanorods. Moreover, the Tafel slopes of polarized CuCo$_2$O$_4$ nanorods are 86.9 mV dec^{-1} in the HER process and 73.1 mV dec^{-1} in the OER process, which are much lower than commercial catalysts of Pt/C (88.0 mV dec^{-1} for HER) or RuO$_2$ (78.5 mV dec^{-1} for OER), proving faster kinetic on polarized CuCo$_2$O$_4$ nanorods due to their higher electroconductibility and intrinsic activity. In particular, polarized CuCo$_2$O$_4$ nanorods are identified as promising catalysts for water electrolysis with robust stability, offering outstanding catalytic performance and excellent energy efficiency.

1. Introduction

Hydrogen (H$_2$) with a high energy density (142 MJ kg^{-1}) is an ideal alternative fuel to replace fossil fuels, which cause energy crisis and environmental pollution.[1–4] It is well known that hydrogen production from water electrolysis, which is driven by waste heat or from renewable energy, is an efficient and promising technology for producing high-purity hydrogen.[5,6] Hitherto, many highly efficient electrocatalysts have been reported for replacing the benchmark platinum (Pt) and iridium/ruthenium dioxide (IrO$_2$/RuO$_2$) catalysts to reduce the energy barrier during the cathodic hydrogen electrolysis reaction (HER) and the anodic oxygen electrolysis reaction (OER) processes over the water electrolyzer. However, the singular binding interaction with key reaction intermediates of those electrocatalysts greatly limits the efficiency of H$_2$ production.[7–9] One promising candidate for breaking this single-surface design is the design of polarized electrocatalysts, by which the polarization direction presents two distinct chemical surfaces.[7] This unique electrocatalyst design with switchable ferroelectric polarization provides an additional mechanism to regulate the vacant and occupied d-orbitals of ferroelectric materials, which causes great interest in the energy conversion field.[10,11]

To date, various ferroelectric catalysts have been exploited for heterogeneous catalysis, showing potential application in oxygen evolution reaction (OER),[12–14] hydrogen evolution reaction (HER),[15–17] oxygen reduction reaction (ORR),[18,19] CO$_2$ electrocatalytic reduction,[20,21] and fuel oxidation,[22,23] which should be ascribed to the effective separation of charges and their subsequent effects. Feng and co-workers believed that the ferroelectricity of Bi$_{1−x}$Sr$_x$FeO$_3$ strengthens the orbitals of Fe 3d and O 2p and facilitates electron transfer on the catalyst/electrolyte interface.[15] Fenning *et al.* reported that upward polarization on well-defined (001) surfaces reduces the work function relative to downward polarization and provides multiple adsorbate interactions, leading to a lower barrier for the HER process.[7] Kou's group also identified several ferroelectric catalysts for controllable CO$_2$ reduction due to their switchable

a Key Laboratory of Eco-chemical Engineering, Ministry of Education, International Science and Technology Cooperation Base of Eco-chemical Engineering and Green Manufacturing, School of Materials Science and Engineering, Qingdao University of Science and Technology, Qingdao 266042, PR China. E-mail: xugrui@gmail.com, inorchemwl@126.com
b College of Chemistry and Molecular Engineering, Qingdao University of Science and Technology, Qingdao 266042, PR China
c Shandong Weima Equipment Science & Technology Co., Ltd., Dongying, 257000, China
† Electronic supplementary information (ESI) available. See DOI: https://doi.org/10.1039/d4nr01320d

polarization regulating the paths of CO_2 reduction and reaction barrier, resulting in different final products.[11] Most of the reported ferroelectric catalysts possess a large particle size and small specific surface area, leading to lesser active site exposure and catalytic performance boundedness. Ferroelectric catalysts with polarization outside the plane and abundant pores inside the plane can be established by layer stacking, which is the necessary condition to obtain true ferroelectric metals with polarization switching and Fermi level non-zero density states.[24,25] Correspondingly, porous structures of ferroelectric catalysts further possess many structural merits for electrocatalysis to boost the charge and electron transfer, catalytic activities, and stability.[26,27]

Given that the catalytic activity relies on the surface active sites and the adsorption of reactants/intermediates and charge transfer, the ferroelectric catalysts with the introduction of pores are promising approaches for generating larger exposed surface area and providing multiple adsorbate interactions that can enhance their catalytic performance.[28] Herein, we synthesized a ferroelectric catalyst of $CuCo_2O_4$ nanorods with a diameter of 4.37 nm, which were polarized by the corona polarization apparatus and denoted as polarized $CuCo_2O_4$ nanorods. Comparing $CuCo_2O_4$ nanorods without polarization, polarized $CuCo_2O_4$ nanorods showed a larger electrochemical surface area (ECSA) and faster electron transfer kinetics that can boost the reaction process of water electrolysis. Meanwhile, by combining multiple adsorbate interactions, the free energy of the key step reaction (ΔG_{max}) was much lower than that of $CuCo_2O_4$ nanorods without polarization. As a result, the polarized $CuCo_2O_4$ nanorods showed an overpotential of the polarized $CuCo_2O_4$ nanorods for HER at 10 mA cm^{-2} was 78.7 mV with a Tafel slope of 86.9 mV dec^{-1}, which was much lower than that of the unpolarized $CuCo_2O_4$ nanorods (161.0 mV and 112.1 mV dec^{-1}) under alkaline conditions. Simultaneously, the polarized $CuCo_2O_4$ nanorods with an overpotential of 299 mV and a Tafel slope of 73.1 mV dec^{-1} at 10 mA cm^{-2} for the OER process were comparable to the commercial RuO_2 (339 mV and 78.5 mV dec^{-1}), indicating superior water splitting activity. Impressively, the electrolyzer of the polarized $CuCo_2O_4$ nanorods||polarized $CuCo_2O_4$ nanorods can be driven by a cell voltage of 1.51 V to reach the current density of 10 mA cm^{-2}, which can maintain well after 35 h of long-time stability tests. This work not only studies in-depth the binding strength of adsorbents and reaction surfaces but also promotes the practical applications of ferroelectric catalysts.

2. Experimental

2.1 Reagents and chemicals

Cobalt nitrate hexahydrate ($Co(NO_3)_2\cdot6H_2O$, ≥99.00%), copper nitrate trihydrate ($Cu(NO_3)_2\cdot3H_2O$, ≥99.99%), Urea (≥99%), and oleic acid were purchased from Aladdin. Ethanol and acetone were purchased from Sinopharm Chemical Reagent Co., Ltd. Deionized water of ≥18 MΩ cm^{-1} was used in all the experiments.

2.2 Synthesis of $CuCo_2O_4$ nanorods

15 mL of ethanol with 10 mL of deionized water and 515.4 mg of urea with 4 mL of oleic acid were combined and stirred for 30 min, referred to as solution A. 10 mL of 86 mmol of $Co(NO_3)_2\cdot6H_2O$ was concentrated with 10 mL of 43 mmol of $Cu(NO_3)_2\cdot3H_2O$, which was called solution B. Solution B was transferred to solution A, stirred for 30 min, and then transferred to a reaction vessel and heated at 180 °C for 9 h, followed by centrifugation for 3 times with acetone and ethanol, and the residue was dried at 60 °C, after which it was air-fired at 400 °C for 3 h.

2.3 Electrochemical measurements

The CHI 660E electrochemical workstation was used for all electrochemical measurements. Cyclic voltammetry (CV) and linear sweep voltammetry (LSV), chrono-potentiometry and chrono-amperometry were carried out in 1M KOH using a conventional three-electrode system. This three-electrode system consisted of a modified glassy carbon electrode (GCE) with a diameter of 3 mm (working electrode area of 0.071 cm^2) as the working electrode, a saturated glycolic electrode (SCE) as the reference electrode and a graphite electrode as the counter electrode. Potentiometric measurements were calibrated to the reversible hydrogen electrode (RHE) according to the equation $E_{RHE} = E_{SCE} + 0.0591$ pH + 0.242. Level values were calibrated by 95% iR compensation of the LSV measurements. Electrocatalytic inks were prepared by adding 10 mg of the prepared catalyst to 5 ml of a mixed solution containing deionized water, isopropanol, and 5% Nafion (V/V/V = 8/2/0.05). Following a 30-minute sonication process, a well-dispersed ink dispersion was obtained. Then, 20 μl of the suspended ink was dropped onto the surface of the working electrode (loading ~0.11 mg cm^{-2}) and dried at room temperature.

2.4 Physical characterization

Transmission electron microscopy (TEM) images were characterised on JEM-2100UHR and EDX analysis was performed at an operating voltage of 200 kV. Scanning electron microscopy (SEM) images were obtained on a Hitachi SU8020 cold emission field emission electron microscope, operating at an accelerating voltage of 5 kV. Atomic force microscopy (AFM) images were collected on a Dimension ICON, Bruker, instrument. X-ray photoelectron spectroscopy (XPS) was carried out on a Kratos AXIS ULTRA using the C 1s peak at 284.5 eV as a reference to correct binding energy. X-ray diffraction (XRD) patterns were collected on a RigakuD/max-2400 instrument to analyse the crystal structure of $CuCo_2O_4$.

3. Results and discussion

The polarized $CuCo_2O_4$ nanorods were prepared by following the steps shown in Scheme 1. Firstly, The Co^{2+} and Cu^{2+} ions precursors were added to the mixed solution combining ethanol, oleic acid, urea, and deionized water. After ultrasonic
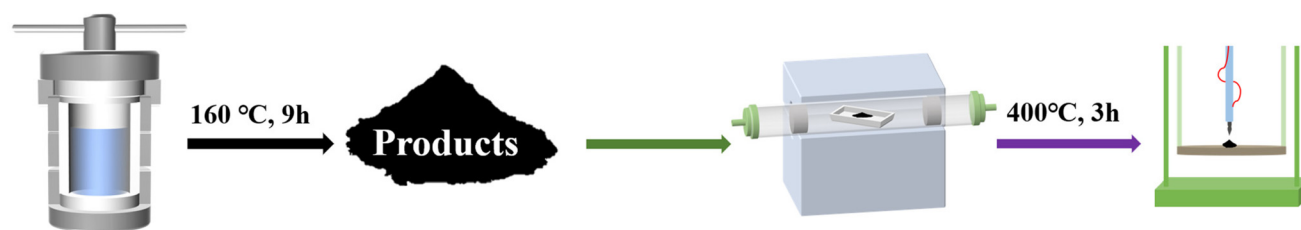
Scheme 1 The preparation process for polarized CuCo$_2$O$_4$ nanorods.

dispersion for 30 min, the above solution was quickly transferred to a stainless steel autoclave (lined with Teflon) and maintained at 180 °C for 9 h. Then, CuCo$_2$O$_4$ nanorods-pre was transferred to a tube furnace, annealing at 400 °C for 3 h. Finally, the obtained CuCo$_2$O$_4$ nanorods were polarized at 22 kV by the corona poling method. The presence of oleic acid inhibits the overgrowth of nanorods and prevents their agglomeration, creating an energy barrier to counteract the adsorption, which can improve the generation of CuCo$_2$O$_4$ nanorods.[29] The crystal structure of the prepared polarized CuCo$_2$O$_4$ nanorods (Fig. 1a) was studied by XRD, which showed a perovskite phase (Fig. 1b). Furthermore, the crystal topology diagram of the polarized CuCo$_2$O$_4$ nanorods is shown in Fig. S1.† Due to the annealing process, repeated measurements in the 2θ range of 5°–90° were performed at high resolution, indicating a high degree of crystallinity. Meanwhile,

CuCo$_2$O$_4$ nanorods after the ferroelectric regulation by corona polarization, the (422) and (533) peaks are significantly higher compared to the corresponding peaks of the unpolarized CuCo$_2$O$_4$ nanorods. The samples before and after polarization showed diffraction peaks at 19.1°, 31.4°, 37.0°, 39.0°, 45.1°, 56.0°, 59.6°, 65.7°, 69.0°, 77.5°, and 83.2°, fitting well with the (111), (220), (311), (222), (400), (422), (511), (440), (531), (533) and (444) lattice planes of cubic CuCo2O4 (JCPDS 01-1155) (Fig. 1a). Both before and after polarization show the same morphology, which confirms that the crystal structure of the sample is not changed after polarization. This crystalline phase change is attributed to the ferroelectric regulation between quasi-electric and ferroelectric in CuCo$_2$O$_4$ nanorods.[30] In addition, the butterfly-shaped amplitude profile revealed by the high-resolution piezoelectric force microscopy (PFM) of the polarized CuCo$_2$O$_4$ nanorods verifies excellent
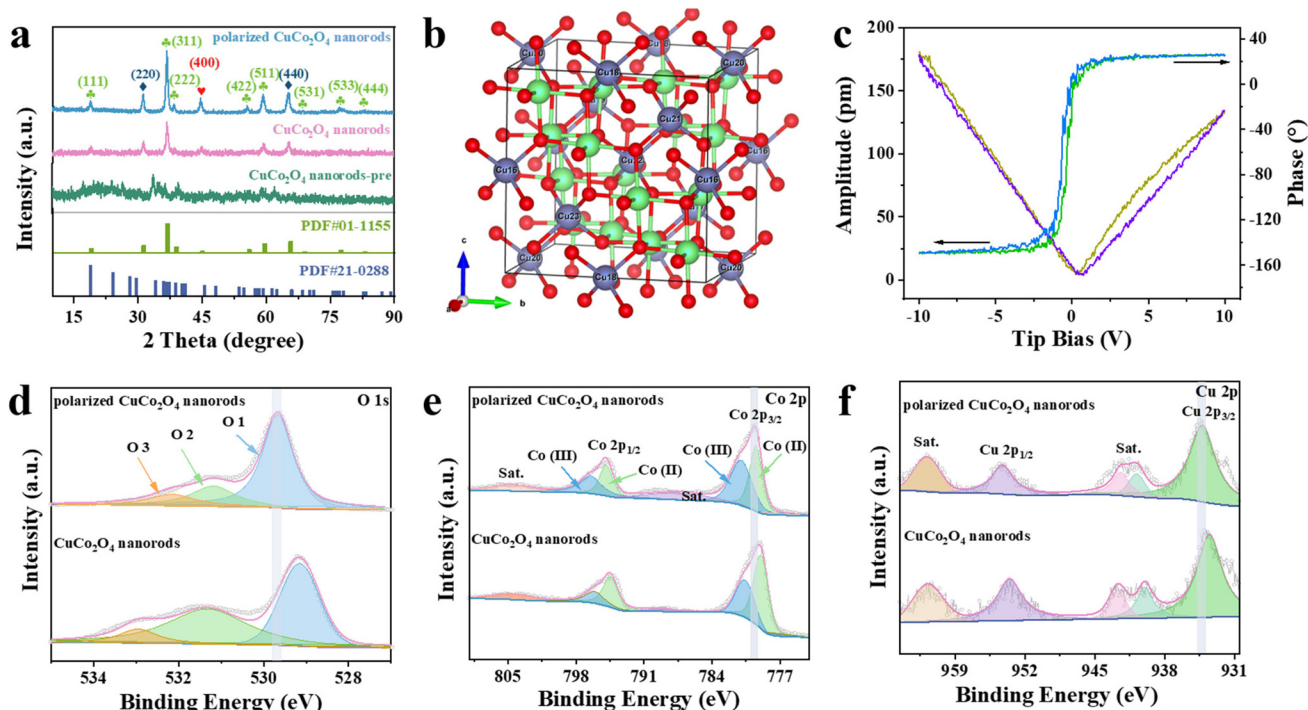

Fig. 1 (a) XRD plots of the polarized CuCo$_2$O$_4$ nanorods, CuCo$_2$O$_4$ nanorods and CuCo$_2$O$_4$ nanorods-pre; (b) crystal structure diagram of the polarized CuCo$_2$O$_4$ nanorods (blue for Cu atoms, green for Co atoms, and red for O atoms); (c) amplitude butterfly loops, and piezoresponse phase hysteresis loops for polarized CuCo$_2$O$_4$ nanorods; (d–f) XPS plots of the polarized CuCo$_2$O$_4$ nanorods and CuCo$_2$O$_4$ nanorods: (d) O 1s; (e) Co 2p; (f) Cu 2p.

local piezoelectric response (Fig. 1c) compared to that in the unpolarized $CuCo_2O_4$ nanorods (Fig. S2†), which further suggests that the polarized samples can maintain their stable ferroelectric switching properties.

The elemental composition and chemical state of polarized $CuCo_2O_4$ nanorods were measured by the X-ray photoelectron spectroscopy (XPS) technique. The full XPS spectrum of the as-prepared polarized $CuCo_2O_4$ nanorods showed distinguishable peaks for the elements of Co, Cu, and O with an atomic ratio of 2.76 : 1.25 : 9.57 (Fig. S3 and S4†), well in agreement with the EDS and ICP-OES measurements (Fig. S5 and Table S1†). As shown in Fig. 1d, the three peaks of O 1s at 532.17, 531.21, and 529.68 eV can be attributed to water molecules, the surface chemisorbed oxygen such as O_2^{2-} or O^-(belonging to defectoxide and the hydroxyl-like group), and metal–oxygen bonds, respectively.[31–33] The Co 3p spectrum can be deconvoluted into two peaks appearing at 779.62 eV and 774.99 eV, associating with the representative peaks of Co $2p_{3/2}$ and Co $2p_{1/2}$, respectively (Fig. 1e).[34] Comparing the peaks of $CuCo_2O_4$ nanorods without polarization, both Co $2p_{3/2}$ and Co $2p_{1/2}$ peaks of the polarized $CuCo_2O_4$ nanorods shift by ~0.50 eV to

higher binding energies, and the increased Co binding energy results in electrons closer to the core, indicating that Co^{2+} has excellent electron trapping ability. The high-resolution Cu 2p spectra in Fig. 1f shows that the peaks at ~941.64 and 961.77 eV are assigned to Cu^{2+} 2p, which positively shifts from the standard binding energies of Cu^{2+} 2p. These suggest that the electron transforms from Cu^{2+} 2p to Co^{2+} 2p.[35,36] This suggests that after polarization, the electrons from the Cu site may migrate to the Co site, the electron density of the Co site increases, and the electrons are first drawn from the Co site for the reaction when the HER and OER reactions are underway, and the Co site can accept the excited electrons and contribute them to the adsorbed intermediates under the effect of polarization, which facilitates the electrolysis of the water reaction.[37]

To elucidate the electron transfer mechanism, the microstructure and morphology of the polarized $CuCo_2O_4$ nanorods were further investigated by SEM and TEM techniques. The smooth surface of $CuCo_2O_4$ nanorods-pre becomes relatively rough after annealing at 400 °C (Fig. S6 and S7†). Simultaneously, the corona polarization process does not affect the morphological structure (Fig. 2a and b). The surface
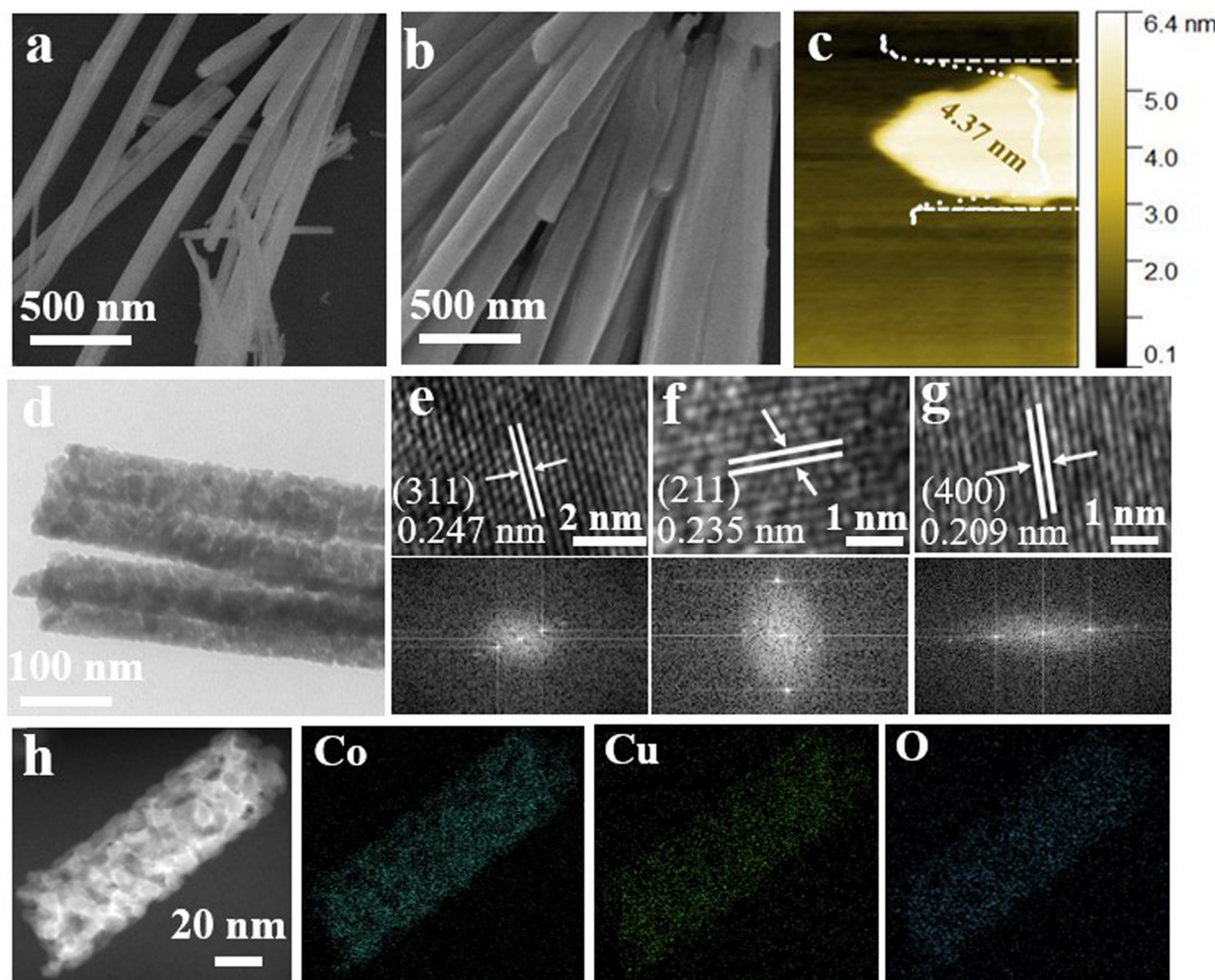

Fig. 2 (a) SEM images of $CuCo_2O_4$ nanorods; (b) SEM images, (c) AFM, (d) TEM, (e–g) partially magnified HRTEM and corresponding FFT images, (h) STEM-EDX elemental mapping maps of polarized $CuCo_2O_4$ nanorods.

area and total pore volume are 31.91 m^2 g^{-1} and 0.17 cm^3 g^{-1} for the polarized CuCo$_2$O$_4$ nanorods as determined by Brunauer–Emmett–Teller (BET) surface area measurements (Fig. S8a and b†), which are higher than those of CuCo$_2$O$_4$ nanorods-pre, indicating a mesoporous structure. The thickness of 4.37 nm for the polarized CuCo$_2$O$_4$ nanorods was further measured by AFM (Fig. 2c) and was well consistent with the above results. A magnified TEM image of the polarized CuCo$_2$O$_4$ nanorods demonstrates the significant porous nanosheet structures (Fig. 2d), providing a large surface area with more exposed active sites. High-resolution TEM (HRTEM) and fast Fourier transform (FFT) images confirm the perovskite crystal structure of polarized CuCo$_2$O$_4$ nanorods. Briefly, the lattice edges of the individual nanorods expose $d(400)$ = 0.209 nm, $d(311)$ = 0.247 nm and $d(211)$ = 0.235 nm crystal spacing, indicating a high degree of crystallinity (Fig. 2e–g). The high-angle annular dark-field scanning transmission electron microscopy (HAADF-STEM) image and their corresponding elemental mapping images demonstrate the uniform distribution of Co, Cu, and O elements in polarized CuCo$_2$O$_4$ nanorods (Fig. 2h), further indicating the composition of crystal CuCo$_2$O$_4$.[38]

The HER performance of the samples was studied on a CHI 660E electrochemical workstation with a standard three-electrode system in 1 M KOH solution. Fig. 3a shows the linear scanning voltammetry (LSV) curves for polarized CuCo$_2$O$_4$ nanorods, CuCo$_2$O$_4$ nanorods, CuCo$_2$O$_4$ nanorods-pre, and 40 wt% Pt/C, where CuCo$_2$O$_4$ nanorods, CuCo$_2$O$_4$ nanorods-pre, and 40 wt% Pt/C serve as the reference samples. It is

obvious that polarized CuCo$_2$O$_4$ nanorods exhibit a higher current density (j) and lower current onset potential than CuCo$_2$O$_4$ nanorods and Pt/C, suggesting that polarization can significantly increase the activity of basic HER. Additionally, the pure nickel foam sample has almost no HER activity under alkaline conditions, suggesting that the activity is mainly derived from surface-loaded metal oxides. The overpotentials at 10 mA cm^{-2}, 50 mA cm^{-2}, and 100 mA cm^{-2} are denoted as η_{10}, η_{50}, and η_{100}, respectively. The η_{10} of the polarized CuCo$_2$O$_4$ nanorods for HER is 78.7 mV, comparable to that of the commercial Pt/C-40% while exhibiting lower η_{50}, and η_{100} values of 138.3 mV and 171.7 mV (Fig. 3b), respectively, which is further superior to most of the state-of-the-art non-noble catalysts reported recently (Table 1), indicating a potential application at a larger current density. Meanwhile, the Tafel slope of the polarized CuCo$_2$O$_4$ nanorods is 86.9 mV dec^{-1}, smaller than that of CuCo$_2$O$_4$ nanorods, CuCo$_2$O$_4$ nanorods-pre, and 40wt% Pt/C (112.1 mV dec^{-1}, 152.6 mV dec^{-1}, and 88.0 mV dec^{-1}) (Fig. 3c), which revealed more favorable reaction kinetics on the polarized CuCo$_2$O$_4$ nanorods. The lower Tafel slope of 86.9 mV dec^{-1} reveals that the reaction process follows the Volmer–Heyrovsky mechanism as the electron polarization reduces the extra $\Delta G(H_2O)$ that boosts the adsorption and activation of H$_2$O. The above results reveal that the polarization process enables a faster HER kinetic rate, implying a lower energy barrier for water dissociation and OH desorption. Moreover, the samples that polarized under different voltages were further provided, which show the same morphological structures while exhibiting different catalytic performance
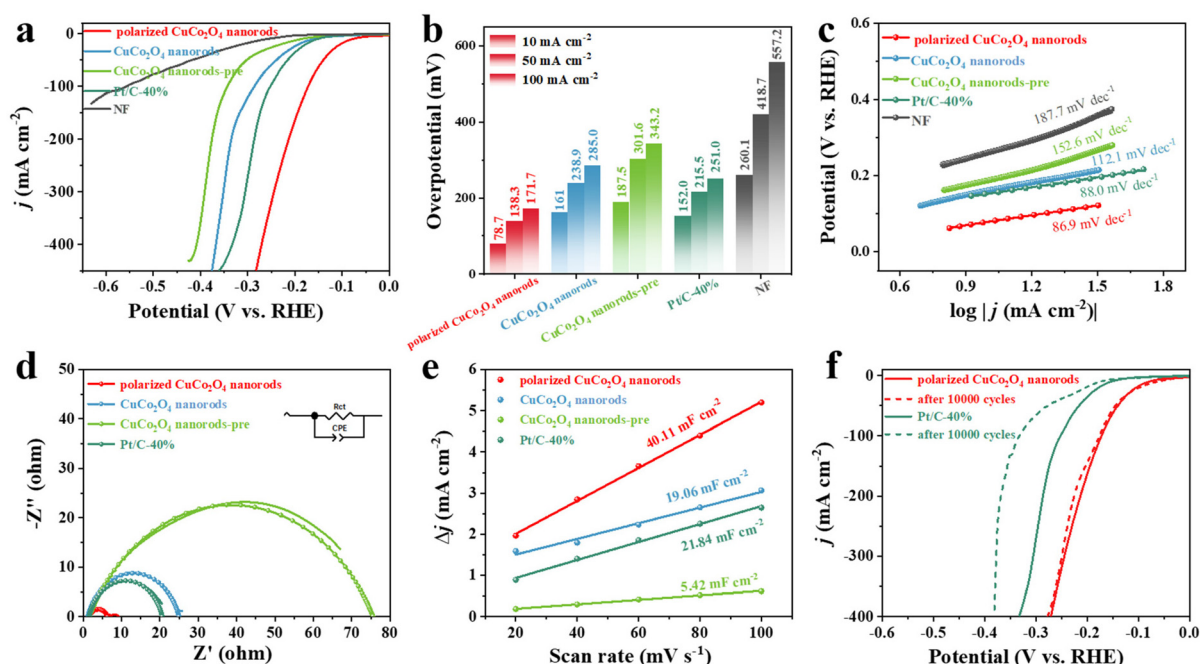

Fig. 3 HER electrocatalytic performance of the polarized CuCo$_2$O$_4$ nanorods, CuCo$_2$O$_4$ nanorods, CuCo$_2$O$_4$ nanorods-pre and commercial Pt/C-40% in 1.0 M KOH solution: (a) LSV polarization curves of HER activity with a scan rate of 5 mV s^{-1}; (b) overpotentials at 10, 50, and 100 mA cm^{-2}; (c) corresponding Tafel plots; (d) Nyquist plots of equivalent circuit models; (e) linear fit of capacitive current to the CV scan rate; (f) LSV polarization curves of the HER activity of the polarized CuCo$_2$O$_4$ nanorods and Pt/C-40% after 10 000 CV cycles.

Table 1 The catalytic performance of non-noble catalysts for HER

Catalyst	Electrolyte	Overpotential mV	Current density mA cm^{-2}	Tafel slope mV dec^{-1}	Ref.
Polarized CuCo$_2$O$_4$ nanorods	1 M KOH	78.7	10	86.9	This work
CuCo$_2$O$_4$/CoOOH/NF	1 M KOH	125	10	75.1	46
P-doped CuCo$_2$O$_4$	1 M KOH	152	10	115.7	47
Ni$_3$S$_2$/FeS	1 M KOH	190	10	56.3	48
Co-MoC/Mo$_2$C	1 M KOH	82	10	53	49
Co$_9$S$_8$@MoS$_2$	1 M KOH	143	10	81.7	50
WP$_2$ NSs/W	1 M KOH	90	10	80.88	51
NiFeP NP supported by carbon	1 M KOH	160	10	75.8	52
Co$_{0.05}$Cu$_{0.05}$@CNWs	1 M KOH	160	10	172	53
Cu–Co–Se	1 M KOH	152	10	94	54
Cu-Ni$_3$S$_2$/Co$_3$S$_4$	1 M KOH	79	10	50.4	55

(Fig. S9, S10†). The polarization voltage of 22 kV used in this work can form a very strong electric field on the surface of the electrode, accelerating the migration rate of electrons and ions, which promotes the electrochemical reaction and increases the rate of electrocatalytic reaction. When the polarization voltage is lower than 22 kV, the polarization effects of samples are not obvious, leading to lower electroconductibility and intrinsic activity of active sites (Fig. S11, S12, S13†).[39–42] When the polarization voltage is higher than 22 kV, samples show similar electroconductibility and intrinsic activity as that polarized under 22 kV (Fig. S11, S12, S13†). Therefore, the high electric field strength can promote the transport of substances in solution, including ions and molecules, which is conducive to increasing the concentration of reactive substances on the electrode surface, enhancing the electrocatalytic reaction. Meanwhile, the active sites after polarization can improve the adsorption of free radicals and reactive oxygen species due to the unique electron effect between Cu and Co atoms.[26,43–45] In addition, the polarization voltage of 22 kV was further widely used in research and industrial production in the field of electrochemistry.

Furthermore, electrochemical impedance spectroscopy (EIS) was used to evaluate the electron transfer kinetics of different catalysts. Among them, polarized CuCo$_2$O$_4$ nanorods showed the lowest charge transfer resistance (R_{ct}) with 4.8 Ω (Fig. 3d), demonstrating its favorable charge transfer ability during the OER process. As an important parameter, the electrochemical active surface area (ECSA) values can determine the intrinsic activity of the catalysts. Therefore, the double-layer capacitance (C_{dl}) was measured by cyclic voltammetry (CV) curves at different scan rates as it was in line with the ECSA value. As shown in Fig. 3e, the C_{dl} of the polarized CuCo$_2$O$_4$ nanorods (40.11 mF cm^{-2}) was significantly higher than those of CuCo$_2$O$_4$ nanorods and CuCo$_2$O$_4$ nanorods-pre (19.06 mF cm^{-2} and 5.42 mF cm^{-2}) grudge matched with commercial Pt/C (21.84 mF cm^{-2}), still displaying the higher intrinsic catalytic activity. Stability is another key factor in the evaluation of electrocatalysts. As shown in Fig. 3f, the polarized CuCo$_2$O$_4$ nanorods electrode showed negligible degradation after 10 000 CV cycles at a rather fast scan rate of 100 mV·s^{-1}, which is outstanding than commercial Pt/C-40%. Meanwhile, the prepared polarized CuCo$_2$O$_4$ nanorods also

showed excellent stability when tested at 10 mA cm^{-2} for 50 h with almost no current density change (Fig. S14†). Moreover, the η_{50} of the polarized CuCo$_2$O$_4$ nanorods negatively shifts 4 mV, which is much smaller than that of CuCo$_2$O$_4$ nanorods (38 mV) (Fig. S15†).

To further explore the OER performance of the polarized CuCo$_2$O$_4$ nanorods, OER polarization curves under alkaline conditions were first tested. As shown in Fig. 4a–c, when compared to CuCo$_2$O$_4$ nanorods, CuCo$_2$O$_4$ nanorods-pre, the polarized CuCo$_2$O$_4$ nanorods exhibited the lowest OER overpotential and Tafel slope of 299 mV and 73.1 mV dec^{-1}, respectively, indicating its superior activity and favorable kinetics process. Furthermore, the overpotential of the polarized CuCo$_2$O$_4$ nanorods at the current density of 100 mA cm^{-2} is 374 mV, which is much lower than that of CuCo$_2$O$_4$ nanorods (397 mV), CuCo$_2$O$_4$ nanorods-pre (393 mV), even commercial RuO$_2$ (408 mV) and most recently reported catalysts (Table 2), demonstrating the superior OER performance of the polarized CuCo$_2$O$_4$ nanorods. Similar to the results for HER, the as-prepared polarized CuCo$_2$O$_4$ nanorods also show outstanding stability when tested at 10 mA cm^{-2} for 35 h with no negligible decay (Fig. S16†). Whereas, the CuCo$_2$O$_4$ nanorods exhibit significant attenuation in 1.0 M KOH solution, revealing the beneficial role of polarization (Fig. S16†). Moreover, the overpotential of the polarized CuCo$_2$O$_4$ nanorods shows a negligible shift at 10 mA cm^{-2} after long-term OER stability tests (Fig. S17†), further indicating excellent OER stability. After the long-term stability test, SEM and TEM scanning and XPS plots of the polarized CuCo$_2$O$_4$ nanorods were further measured (Fig. S18, S19, S20†) which showed no significant changes compared to the initial polarized CuCo$_2$O$_4$ nanorods, further confirming their excellent stability.

Due to their good OER and HER performance, polarized CuCo$_2$O$_4$ nanorods can serve as a bifunctional electrode catalyst for an overall water electrolyzer. The difference corresponding to the overpotentials of HER and OER polarization curves ($\Delta E = \eta_{OER} + \eta_{HER}$) at various current densities was used to evaluate the performance of the water electrolyzer. The ΔE value of the polarized CuCo$_2$O$_4$ nanorods at the current densities of 10 mA cm^{-2} is 1.61 V, exhibiting a strong prospect in water splitting application (Fig. 4d). Based on the good catalytic activity for OER and HER in 1.0 M KOH solution, polar-
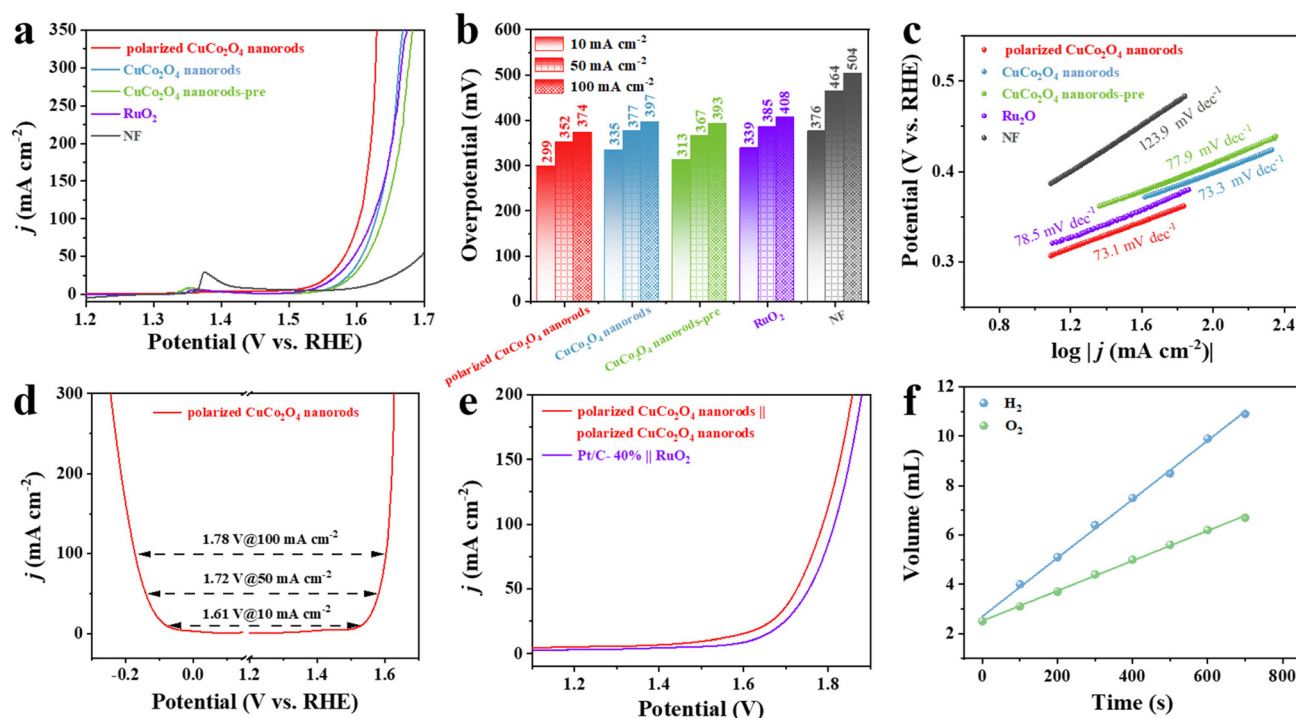
Fig. 4 OER electrocatalytic performance of the polarized $CuCo_2O_4$ nanorods, $CuCo_2O_4$ nanorods, $CuCo_2O_4$ nanorods-pre and commercial RuO_2 in 1.0 M KOH solution: (a) LSV polarization curves of OER activity with a scan rate of 5 mV s^{-1}; (b) overpotentials at 10, 50, and 100 mA cm^{-2}; (c) corresponding Tafel plots; (d) ΔE values of polarized $CuCo_2O_4$ nanorods at 10, 50, and 100 mA cm^{-2} current densities; (e) LSV polarization curves for polarized $CuCo_2O_4$ nanorods/NF($\pm$) and RuO_2/NF(+)||Pt/C-40%/NF(−); (f) curves of H_2 and O_2 produced by polarized $CuCo_2O_4$ nanorods/NF($\pm$) as a function of time.

Table 2 The catalytic performance of non-noble catalysts for OER

Catalyst	Electrolyte	Overpotential mV	Current density mA cm^{-2}	Tafel slope mV dec^{-1}	Ref.
Polarized $CuCo_2O_4$ nanorods	1 M KOH	299	10	73.1	This work
FeCoCNFs	1 M KOH	377	10	59.9	56
CoNC/NCNTs@CNF	1 M KOH	330	10	82	57
Co-ZIF-350-air micro-fibers	1 M KOH	370	10	55	58
Fe_2O_3/$NiFe_2O_4$@CNFs-2	1 M KOH	350	10	51.4	59
h-Co_3O_4/CeO_2@N-CNF	1 M KOH	310	10	85	60
CuCoO/S-CP-Ar-30	0.1 M KOH	330	10	114.9	61
Fe-CoO/C-800 nanofibers	1 M KOH	362	10	60	62
Ti_3C_2Tx/$CuCo_2O_4$/NF	1 M KOH	360	10	49	63
Ti_3C_2Tx/$CuCo_2O_4$/GC	1 M KOH	380	10	71	63
NiCo-500-15	1 M KOH	320	10	67	64

ized $CuCo_2O_4$ nanorods were further tested for the overall decomposition performance of polarized $CuCo_2O_4$ nanorods as a two-electrode system for both anode and cathode on an overall water decomposition device (Fig. 4e). As shown in Fig. 4e, the cell voltages of the polarized $CuCo_2O_4$ nanorods at the current densities of 10, 50, and 100 mA cm^{-2} are only 1.51 V, 1.72 V, and 1.78 V, respectively, which is second only to the latest electrolyzer consisting of RuO_2/NF(+) and Pt/C-40%/NF(−) (1.62 V, 1.75 V, and 1.81 V), confirming that polarized $CuCo_2O_4$ nanorods possess excellent HER and OER activities. These results show that polarized $CuCo_2O_4$ nanorods/NF can effectively serve as both anode and cathode material and are

very effective in reducing the total water cracking tank potential. Furthermore, the long-term stability of the optimum electrolyzer-polarized $CuCo_2O_4$ nanorods/NF($\pm$) was evaluated through a chrono-current (CA) stability test. The polarized $CuCo_2O_4$ nanorods/NF($\pm$) electrolyzer exhibited high stability, with no significant change in the initial current density compared to the current density after the 35 hour stability test (Fig. S21†). Simultaneously, the LSV curves show that there is almost no change after the long-term stability tests, suggesting excellent durability (Fig. S22†). Fig S23† shows the precipitation of H_2 at the cathode and O_2 at the anode during the operation of the polarized $CuCo_2O_4$ nanorods/NF($\pm$) electroly-

zer, which indicates that bubbles can be effectively shunted off the electrode surface due to the high porosity of the electrodes without significant accumulation of bubbles on the electrode surface. The volume of H_2 and O_2 produced on the cathode and anode with polarized $CuCo_2O_4$ nanorods-based water electrolyzer was evaluated by the drainage method. As shown in Fig. S24,† the volume of O_2 and H_2 increases with the reaction process and agrees well with the large number of bubbles generated on the electrodes (Fig. S23†). The output ratio of O_2 and H_2 is about $1:1.95$, close to the theoretical value of $1:2$ (Fig. 4f), which confirms that the faradaic efficiency (FE) is close to 100%. Overall, the electrochemical evaluation of HER, OER, and overall water splitting confirm the strong potential of polarized $CuCo_2O_4$ nanorods for practical applications with low cost.

4. Conclusion

In conclusion, we have certified the electronic polarization of the polarized $CuCo_2O_4$ nanorods with a thickness of 4.37 nm, which may be related to their state density. Owing to the optimized electron polarization, polarized $CuCo_2O_4$ nanorods exhibit remarkable HER and OER performance, greatly superior to that of $CuCo_2O_4$ nanorods and almost as good as the best commercial Pt/C-40% catalysts. In particular, polarized $CuCo_2O_4$ nanorods showed the highest electrocatalytic HER activity under alkaline conditions for both overpotential and Tafel slope, which were 138.3 mV at 50 mA cm^{-2} and 86.9 mV dec^{-1} at 10 mA cm^{-2}, respectively, far exceeding the sample of $CuCo_2O_4$ nanorods without polarization. More importantly, when employed as the cathode and anode of the water electrolyzer, the polarized $CuCo_2O_4$ nanorods/NF(±) just required a cell voltage of 1.51 V to achieve the current density of 10 mA cm^{-2}. This work presents a novel idea for evaluating electron polarization in improving the mass and electron transfer on the interface of electrode/electrolyte, and it opens up a new strategy for obtaining a low-cost and high-performance water electrolyzer.

Conflicts of interest

The authors declare that they have no known competing financial interests or personal relationships that could have appeared to influence the work reported in this paper.

Acknowledgements

References

1 L. Yu, Q. Zhu, S. Song, B. McElhenny, D. Wang, C. Wu, Z. Qin, J. Bao, Y. Yu, S. Chen and Z. Ren, *Nat. Commun.*, 2019, **10**, 5106.

2 T. I. Singh, G. Rajeshkhanna, U. N. Pan, T. Kshetri, H. Lin, N. H. Kim and J. H. Lee, *Small*, 2021, **17**, 2101312.

3 P. Zhou, G. Zhai, X. Lv, Y. Liu, Z. Wang, P. Wang, Z. Zheng, H. Cheng, Y. Dai and B. Huang, *Appl. Catal., B*, 2021, **283**, 100–105.

4 W. Moschkowitsch, O. Lori and L. Elbaz, *ACS Catal.*, 2022, **12**, 1082–1089.

5 Y. Liu, J. Guan, W. Chen, Y. Wu, S. Li, X. Du and M. Zhang, *J. Alloys Compd.*, 2022, **891**, 161790.

6 L. Fang, Z. Jiang, H. Xu, L. Liu, Y. Guan, X. Gu and Y. Wang, *J. Catal.*, 2018, **357**, 238–246.

7 P. Abbasi, M. R. Barone, M. de la Paz Cruz-Jáuregui, D. Valdespino-Padilla, H. Paik, T. Kim, L. Kornblum, D. G. Schlom, T. A. Pascal and D. P. Fenning, *Nano Lett.*, 2022, **22**, 4276–4284.

8 X. Du, C. Zhang, H. Wang, Y. Wang and X. Zhang, *J. Alloys Compd.*, 2021, **885**, 10.

9 B. He, G. Pan, Y. Deng, L. Zhao, H. Wang, R. Wang and Y. Gong, *Appl. Surf. Sci.*, 2021, **569**, 9.

10 H. Wang, X. Liu, P. Niu, S. Wang, J. Shi and L. Li, *Matter*, 2020, **2**, 1377–1413.

11 L. Ju, X. Tan, X. Mao, Y. Gu, S. Smith, A. Du, Z. Chen, C. Chen and L. Kou, *Nat. Commun.*, 2021, **12**, 5128.

12 S. Wang, Q. Li, S. Sun, K. Ge, Y. Zhao, K. Yang, Z. Zhang, J. Cao, J. Lu, Y. Yang, Y. Zhang, M. Pan, Z. Lin and L. Zhu, *J. Mater. Chem. A*, 2022, **10**, 5350–5360.

13 Y. Zhang, M. Yang, X. Jiang, W. Lu and Y. Xing, *J. Alloys Compd.*, 2020, **818**, 7.

14 W. Sun, X. Ling, W. Wei, H. Hu, Z. Jiang, Z. Yan and J. Xie, *Appl. Surf. Sci.*, 2019, **493**, 710–718.

15 J. Qi, H. Liu, M. Feng, H. Xu, H. Liu, C. Wang, A. Wang and W. Lü, *J. Energy Chem.*, 2021, **53**, 93–98.

16 J. P. Hughes, J. Clipsham, H. Chavushoglu, S. J. Rowley Neale and C. E. Banks, *Renewable Sustainable Energy Rev.*, 2021, **139**, 17.

17 X. K. Huang, X. P. Xu, C. Li, D. F. Wu, D. J. Cheng and D. P. Cao, *Adv. Energy Mater.*, 2019, **9**, 10.

18 C. Z. Wan, X. F. Duan and Y. Huang, *Adv. Energy Mater.*, 2020, **10**, 19.

19 X. L. Tian, X. F. Lu, B. Y. Xia and X. W. Lou, *Joule*, 2020, **4**, 45–68.

20 D. Yang, B. Ni and X. Wang, *Adv. Energy Mater.*, 2020, **10**, 7.

21 W. Shan, R. Liu, H. Zhao, Z. He, Y. Lai, S. Li, G. He and J. Liu, *ACS Nano*, 2020, **14**, 11363–11372.

22 Y. Zheng, X. J. Wan, X. Cheng, K. Cheng, Z. F. Dai and Z. H. Liu, *Catalysts*, 2020, **10**, 22.

23 C. Liu, W. Zhou, J. F. Zhang, Z. L. Chen, S. L. Liu, Y. Zhang, J. X. Yang, L. Y. Xu, W. B. Hu, Y. N. Chen and Y. D. Deng, *Adv. Energy Mater.*, 2020, **10**, 8.

24 T. L. Wan, L. Ge, Y. Pan, Q. Yuan, L. Liu, S. Sarina and L. Kou, *Nanoscale*, 2021, **13**, 7096–7107.

25 S. L. Guo, S. N. Lai and J. M. Wu, *ACS Nano*, 2021, **15**, 16106–16117.

26 M. Y. Yan, Z. D. Xiao, J. J. Ye, X. Yuan, Z. H. Li, C. Bowen, Y. Zhang and D. Zhang, *Energy Environ. Sci.*, 2021, **14**, 61586190.

27 L. Zhang, C. Tang, S. Sanvito and A. J. Du, *Mater. Horiz.*, 2023, **10**, 2599–2608.

28 H. Khan, J. Ahmed, S. E. Lofland, K. V. Ramanujachary and T. Ahmad, *Mater. Today Chem.*, 2023, **33**, 10.

29 Y. Zhou, L. Ma, M. Gan, M. Ye, X. Li, Y. Zhai, F. Yan and F. Cao, *Appl. Surf. Sci.*, 2018, **444**, 1–9.

30 S. G. Mohamed, I. Hussain, M. S. Sayed and J.-J. Shim, *J. Alloys Compd.*, 2020, **842**, 9.

31 Y. S. Park, M. J. Jang, J. Jeong, S. M. Park, X. Wang, M. H. Seo, S. M. Choi and J. Yang, *ACS Sustainable Chem. Eng.*, 2020, **8**, 2344–2349.

32 P. Zhang and H. He, *J. Alloys Compd.*, 2020, **826**, 8.

33 W. Li, H. Zhang, M. Hong, L. Zhang, X. Feng, M. Shi, W. Hu and S. Mu, *Chem. Eng. J.*, 2022, **431**, 10.

34 J. Sun, X. Du, R. Wu, Y. Zhang, C. Xu and H. Chen, *ACS Appl. Energy Mater.*, 2020, **3**, 8026–8037.

35 S. M. Pawar, B. S. Pawar, P. T. Babar, A. T. A. Ahmed, H. S. Chavan, Y. Jo, S. Cho, J. Kim, B. Hou, A. I. Inamdar, S. Cha, J. H. Kim, T. G. Kim, H. Kim and H. Im, *Appl. Surf. Sci.*, 2019, **470**, 360–367.

36 X. Hu, S. Liu, Y. Wang, X. Huang, J. Jiang, H. Cong, H. Lin and S. Han, *J. Colloid Interface Sci.*, 2021, **600**, 72–82.

37 S. Zhu, X. Li, X. Jiao, W. Shao, L. Li, X. Zu, J. Hu, J. Zhu, W. Yan, C. Wang, Y. Sun and Y. Xie, *Nano Lett.*, 2021, **21**, 2324–2331.

38 G. R. Reddy, B. Sravani, N. Jung, G. R. Dillip and S. W. Joo, *ACS Appl. Mater. Interfaces*, 2023, **15**, 36500–36511.

39 Y. Ren, L. Hu, S. Chang, Y. Ma, B. Wang, H. Wu, F. Li, Y. Yang, S. Tang and X. J. S. Meng, *Small*, 2024, 2400068.

40 D. Shao, T. Wu, X. Li, X. Ren and Z. J. S. S. Xu, *Small*, 2023, **3**, 2300065.

41 S. Li, L. Bai, N. Ji, S. Yu, S. Lin, N. Tian and H. J. o. M. C. A. Huang, *J. Mater. Chem. A*, 2020, **8**, 9268–9277.

42 J. Xu, X.-X. Xue, G. Shao, C. Jing, S. Dai, K. He, P. Jia, S. Wang, Y. Yuan and J. N. C. Luo, *Nat. Commun.*, 2023, **14**, 7849.

43 L. Liu, J. Hu, Z. Ma, Z. Zhu, B. He, F. Chen, Y. Lu, R. Xu, Y. Zhang and T. J. N. C. Ma, *Angew. Chem., Int. Ed.*, 2024, **15**, 305.

44 H. Yu, F. Chen, X. Li, H. Huang, Q. Zhang, S. Su, K. Wang, E. Mao, B. Mei and G. J. N. c. Mul, *Nat. Commun.*, 2021, **12**, 4594.

45 T. Lv, J. Li, N. Arif, L. Qi, J. Lu, Z. Ye and Y.-J. J. M. Zeng, *Matter*, 2022, **5**, 2685–2721.

46 C. Wang, H. Jiu, L. Zhang, W. Song, Y. Zhang, H. Wei, Q. Xu, S. Che, Z. Guo and Y. Qin, *J. Alloys Compd.*, 2022, **929**, 167367.

47 S. Tan, Y. Ji, F. Ren, F. Chen and W. Ouyang, *Int. J. Hydrogen Energy*, 2022, **47**, 9248–9260.

48 K. Xiao, J.-X. Wei, W.-K. Han and Z.-Q. Liu, *J. Power Sources*, 2021, **487**, 229408.

49 J. Li, R. Ge, P. Lan, J. Yang, J. Feng, Y. Li, S. Li, B. Liu and W. Li, *J. Mater. Chem. A*, 2022, **10**, 10493–10502.

50 M. Kim, M. A. R. Anjum, M. Choi, H. Y. Jeong, S. H. Choi, N. Park and J. S. Lee, *Adv. Funct. Mater.*, 2020, **30**, 2002536.

51 Q. Qin, J. Li, Z. G. Guo, C. Y. Jian and W. Liu, *Int. J. Hydrogen Energy*, 2019, **44**, 27483–27491.

52 Q. L. Kang, M. Y. Li, J. W. Shi, Q. Y. Lu and F. Gao, *ACS Appl. Mater. Interfaces*, 2020, **12**, 19447–19456.

53 Z. K. Ghouri, A. Badreldin, K. Elsaid, D. Kumar, K. Youssef and A. Abdel-Wahab, *J. Ind. Eng. Chem.*, 2021, **96**, 243–253.

54 Z. Z. Ma, X. D. Gu, G. Liu, Q. Zhao, J. P. Li and X. G. Wang, *ChemSusChem*, 2021, **14**, 5065–5074.

55 H. Su, S. Song, S. Li, Y. Gao, L. Ge, W. Song, T. Ma and J. Liu, *Appl. Catal., B*, 2021, **293**, 120225.

56 E. Heo, S. Noh, H. Jo, H. Lee, S. Lee, M. Kim, J. Lee and H. Yoon, *ACS Appl. Nano Mater.*, 2021, **4**, 11031–11041.

57 X. Yao, J. Li, Y. Zhu, L. Li and W. Zhang, *Composites, Part B*, 2020, **193**, 108058.

58 S. S. Sankar, S. R. Ede, S. Anantharaj, K. Karthick, K. Sangeetha and S. Kundu, *Catal. Sci. Technol.*, 2019, **9**, 1847–1856.

59 X. Meng, J. Xie, Y. Sun, J. Liu, B. Liu, R. Wang, F. Ma, M. Liu and J. Zou, *Int. J. Hydrogen Energy*, 2022, **47**, 21329–21343.

60 T. Li, S. Li, Q. Liu, Y. Tian, Y. Zhang, G. Fu and Y. Tang, *ACS Sustainable Chem. Eng.*, 2019, **7**, 17950–17957.

61 J. Zheng, D. Meng, J. Guo and Z. Wang, *J. Alloys Compd.*, 2023, **968**, 172254.

62 W. Li, M. Li, C. Wang, Y. Wei and X. Lu, *Appl. Surf. Sci.*, 2020, **506**, 144680.

63 S. Ghorbanzadeh, S. A. Hosseini and M. Alishahi, *J. Alloys Compd.*, 2022, **920**, 165811.

64 C. Zhang, B. Xin, T. Chen, H. Ying, Z. Li and J. Hao, *Green Energy Environ.*, 2022, **7**, 1217–1227.